

COMBINED *STEREO*/*RHESSI* STUDY OF CORONAL MASS EJECTION ACCELERATION AND PARTICLE ACCELERATION IN SOLAR FLARES

M. TEMMER¹, A. M. VERONIG¹, E. P. KONTAR², S. KRUCKER³, AND B. VRŠNAK⁴

¹ IGAM/Kanzelhöhe Observatory, Institute of Physics, Universität Graz, Universitätsplatz 5, A-8010 Graz, Austria; mat@igam.uni-graz.at, asv@igam.uni-graz.at

² Department of Physics and Astronomy, University of Glasgow, Glasgow G12 8QQ, UK; eduard@astro.gla.ac.uk

³ Space Sciences Laboratory, University of California, Berkeley, CA 94720-7450, USA; krucker@ssl.berkeley.edu

⁴ Hvar Observatory, Faculty of Geodesy, University of Zagreb, Kačićeva 26, HR-10000 Zagreb, Croatia; bvršnak@gmail.com

Received 2009 July 17; accepted 2010 February 15; published 2010 March 15

ABSTRACT

Using the potential of two unprecedented missions, *Solar Terrestrial Relations Observatory (STEREO)* and *Reuven Ramaty High-Energy Solar Spectroscopic Imager (RHESSI)*, we study three well-observed fast coronal mass ejections (CMEs) that occurred close to the limb together with their associated high-energy flare emissions in terms of *RHESSI* hard X-ray (HXR) spectra and flux evolution. From *STEREO*/EUVI and *STEREO*/COR1 data, the full CME kinematics of the impulsive acceleration phase up to $\sim 4 R_{\odot}$ is measured with a high time cadence of ≤ 2.5 minutes. For deriving CME velocity and acceleration, we apply and test a new algorithm based on regularization methods. The CME maximum acceleration is achieved at heights $h \leq 0.4 R_{\odot}$, and the peak velocity at $h \leq 2.1 R_{\odot}$ (in one case, as small as $0.5 R_{\odot}$). We find that the CME acceleration profile and the flare energy release as evidenced in the *RHESSI* HXR flux evolve in a synchronized manner. These results support the “standard” flare/CME model which is characterized by a feedback relationship between the large-scale CME acceleration process and the energy release in the associated flare.

Key words: Sun: coronal mass ejections (CMEs) – Sun: flares – Sun: X-rays, gamma rays

1. INTRODUCTION

Solar flares and coronal mass ejections (CMEs) are the most violent phenomena in our solar system. Many aspects of the basic physics of these events are still not well understood. In the “standard” model, it is envisaged that the erupting filament or CME stretches the coronal magnetic field lines to build up a vertical current sheet, where magnetic reconnection sets in to explosively release vast amounts of free magnetic energy, previously stored in the corona in non-potential magnetic fields (for a review, see, e.g., Forbes 2000). The released energy goes into plasma heating, acceleration of particles to suprathermal velocities, as well as into kinetic energy of the eruption. In this model, a close relation between the kinematics of the CME and the energy release in the associated flare is expected.

A significant fraction of the primary flare energy goes directly into acceleration of fast electrons (e.g., Hudson et al. 1992). As the accelerated electrons precipitate downward along the newly closed magnetic field lines to the lower lying denser atmospheric layers, they are collisionally stopped, and they heat and ionize the chromosphere and lower transition region. This can then be observed as enhanced UV and $H\alpha$ radiation. If the beam flux is high enough, they will also emit detectable hard X-rays (HXRs) via non-thermal bremsstrahlung when the electrons scatter off ions of the ambient thermal plasma. Thus, HXR emission provides the most direct indicator of the evolution of the energy release in a flare (e.g., Fletcher & Hudson 2001).

Several authors found a correlation between the CME acceleration and the flare soft X-ray (SXR) emission (Zhang et al. 2001, 2004; Zhang & Dere 2006; Vršnak et al. 2004, 2007; Maričić et al. 2007). In a recent case study by Temmer et al. (2008), an almost synchronized behavior between CME acceleration and flare HXR emission was obtained for two on-disk events. Such results reveal that, for some associated flare-CME

events, the reconnection process during the flare is closely related to the CME kinematical evolution. The question remains if it is also possible to relate the flare HXR emission (count rate and spectral parameters) to the CME acceleration magnitude. The *Reuven Ramaty High-Energy Solar Spectroscopic Imager (RHESSI)*; Lin et al. 2002) delivers HXR spectra and images at high temporal and spectral resolution, which enables us to study in detail the flare energy release process.

To study the flare energy release in relation to the CME kinematics, the impulsive or main acceleration phase of a CME has to be covered. Since the impulsive acceleration phase of a CME takes place at distances of $R \lesssim 3 R_{\odot}$ (MacQueen & Fisher 1983; St. Cyr et al. 1999; Vršnak 2001; Zhang et al. 2001; Temmer et al. 2008), observations at low coronal heights and of high temporal cadence are required but are only limited available from white-light coronagraphs. The Extreme Ultraviolet Imager instruments aboard the twin spacecraft of the *Solar Terrestrial Relations Observatory (STEREO)*; Kaiser et al. 2008) mission have a large field of view (FoV) and a high time resolution in the 171 Å passband, perfectly suiting such studies. Together with COR1 observations from the inner coronagraph on board *STEREO*, the impulsive acceleration phase of a CME is fully covered from its launch in the low corona up to $4.0 R_{\odot}$.

In this paper, we study and analyze the CME dynamics and HXR emission of the associated flare for three well-observed CME/flare events, using the potential of two unprecedented missions, *STEREO* and *RHESSI*. The events are selected to be located close to the limb in order to minimize the effect of projection in the CME kinematics. In addition, we apply a new algorithm (based on regularization methods) to derive the CME velocity and acceleration from the measured height–time (HT) data. A systematic test of the regularization method as well as a least-squares spline algorithm to a variety of synthetic CME acceleration profiles is performed, in order to evaluate the limitations and uncertainties of both methods.

2. DATA AND METHODS

The Sun Earth Connection Coronal and Heliospheric Investigation (SECCHI; Howard et al. 2008) instrument package is a part of each of the *STEREO* twin spacecraft, *STEREO-A* (ahead) and *STEREO-B* (behind). It includes among others the Extreme Ultraviolet Imager (EUVI; Wuelser et al. 2004) and the white-light inner coronagraph COR1 (Thompson et al. 2003). EUVI has a FoV of $1.7 R_{\odot}$ which enables us to follow the erupting CME structure during its initiation and early propagation phase. Combining EUVI with COR1 observations, which have a FoV of $1.4\text{--}4.0 R_{\odot}$, we can derive a complete velocity and acceleration profile for the early CME evolution. The partially overlapping FoVs between EUVI and COR1 allow us to check if the same features are followed in both instruments.

Further advantages are the high time cadence of EUVI and COR1 observations which allow us to study the evolution of impulsive CME events low in the corona. EUVI observes in the EUV 171 Å passband (Fe x, xi: $T \sim 1 \times 10^6$ K) with a nominal cadence of 2.5 minutes; COR1 has a cadence of 10 minutes. Each day during 18:00–22:00 UT, EUVI, and COR1 gather observations with increased cadence, namely 75 s for EUVI and 5 minutes for COR1 in order to coordinate with Mauna Loa Solar Observatory as well as during observing campaigns. For the study of the CME kinematics, we combine EUVI 171 Å filtergrams and total brightness images calculated from COR1 polarization sequence triplets. The level-0 data are properly reduced using SolarSoft routines, and all images are background subtracted (for COR1, monthly background is subtracted from each polarization component) and rotated to solar north up.

RHESSI performs imaging spectroscopy of solar flares in the energy range from 3 keV to 17 MeV with high temporal, spatial, and spectral resolution (Lin et al. 2002). The flares under study are fully covered with *RHESSI* observations during their peak phase which enables us to study in detail their HXR spectra and flux evolution in relation to the kinematics of the associated CMEs. *RHESSI* spectra were integrated over 20 s during the flare peak with a spectral resolution of 1 keV and fitted with a thermal plus non-thermal power-law component using OSPEX (Schwartz et al. 2002). From the power-law component, we derive the amplitude of the HXR photon spectrum at 50 keV, the spectral index γ of the photon spectrum (slope of the power law), and the power in electrons above a cutoff energy of 25 keV for thick-target emission (Brown 1971). *RHESSI* images were reconstructed during the flare peak using the CLEAN algorithm (Hurford et al. 2002) including front detectors 2–8 (except 5 and 7).

3. DERIVATION AND TEST OF CME ACCELERATION PROFILES

For our study, the reliable derivation of CME velocity and acceleration profiles from the measured HT data is crucial. The central problem is to properly smooth the noisy data and to estimate the impact of measurement errors on the derived quantities, especially on the acceleration profile. This issue received a lot of attention for deriving CME kinematical curves from *Solar and Heliospheric Observatory (SOHO)*/Large Angle and Spectrometric Coronagraph Experiment (LASCO) data (see Wen et al. 2007). Here, we apply a new type of technique to derive velocity and acceleration profiles from HT measurements, namely, an enhanced regularization algorithm originally developed by Kontar et al. (2004) to invert solar X-ray spectra measured by *RHESSI*.

The main problem of time derivatives of data with measurement errors is that its finite difference estimate always leads to an amplification of the error. This can be expressed as the sum of discretization (finite time cadence) and propagation errors (Groetsch 1984). The former error is proportional to the time cadence of the measurements, while the latter is inversely proportional to it. Therefore, the total derivative error always has a minimum (Hanke & Scherzer 2001). Following Hanke & Scherzer (2001) and Kontar & MacKinnon (2005), the regularized method searches for a model-independent velocity and acceleration estimate (regularized solution) with a minimum error, which produces smooth derivatives and avoids additional errors typical of finite differences. In addition, the regularized method of Kontar & MacKinnon (2005) provides the confidence interval for the first and second derivatives, i.e., for CME velocity and acceleration profiles. The outcome of the regularization algorithm is controlled by two parameters. The number of time bins (which has a smoothing effect) and the regularization “tweak,” an important parameter that regulates how reliable are the uncertainties of the input data (e.g., “tweak” of one means that the errors follow a normal distribution without systematics or correlation).

To test the reliability of the results, we compare the CME acceleration profiles⁵ derived from the regularization algorithm with those derived from a least-squares spline fit method, which is an advanced method already used in previous CME studies (Maričić et al. 2004; Vršnak et al. 2007). (Note that we did not compare less-sophisticated methods, like direct derivation of the HT data or three-point Lagrangian interpolation, since these would give worse results.) Based on the formulas given in Gallagher et al. (2003), we generate synthetic kinematical curves of CME propagation representing different scenarios of CME evolution (impulsive and gradual acceleration profiles).

We then reduce the sampling rate of the generated curve and add some noise. The noise consists of random noise as well as of manually shifting individual data points. With this, we aim to take into account the decrease in the dynamic range of CME observations from the inner to the outer corona as well as inconsistencies of tracking features across different wavelength regimes (EUV and white light). From these “imperfect” data points, the acceleration profile is derived and compared to the acceleration profile from the original “perfect” synthetic curve using the regularization and the spline method. To test the stability of the two methods, we simulate HT data with different errors and sampling rates. For both methods, the normalized residuals are derived, i.e., the differences between the measured HT values and the values resulting from the fitting procedure and the regularized solution, respectively, divided by the error.

In addition to the regularization method, we use the spline fit routine which computes least-squares splines with equally spaced nodes to the HT data points (SPLFIT in IDL). From the spline fit curve, we numerically derive the second-order derivative to determine the acceleration. The smoothing effect of the spline fit is controlled by the number of nodes n (e.g., Vršnak et al. 2007). To illustrate the way in which this affects the shape of the derived acceleration curve, we present the results of the spline fit for three different numbers of nodes ($n - 1$, n , $n + 1$). The nodes are chosen in such a way that the residuals for each of the curves would be equally small.

⁵ Deriving the acceleration profile, i.e., calculating the second derivative, highly intensifies noise on the data. The outcome of the acceleration is critical in order to reliably compare with HXR emission.

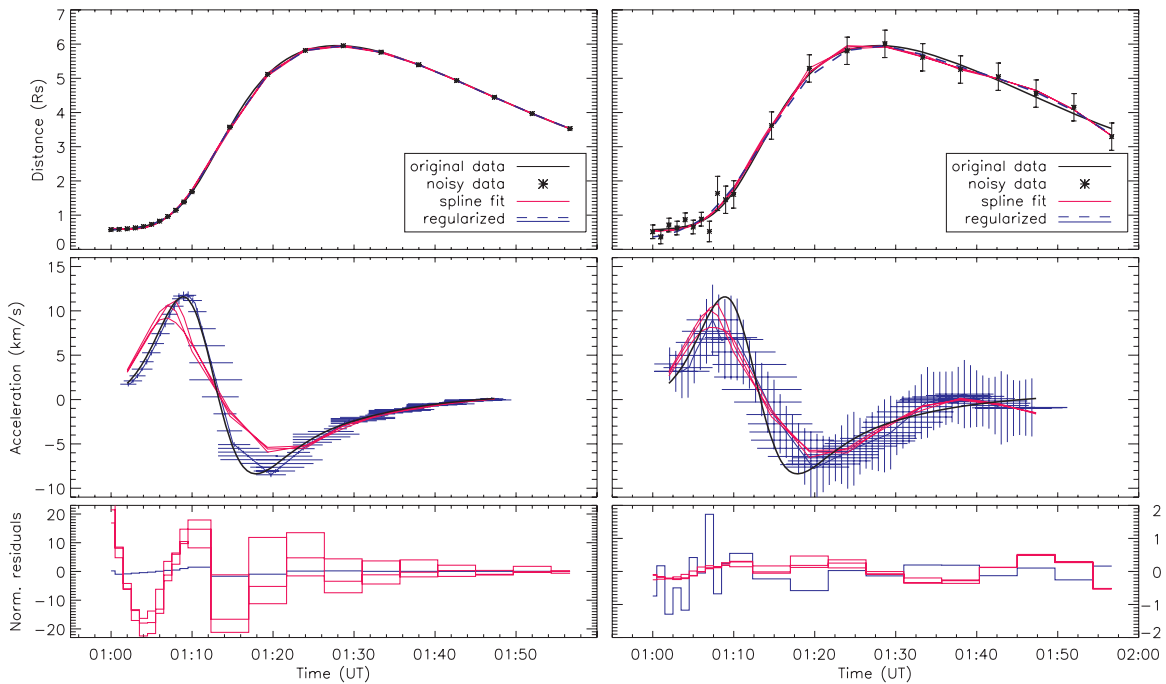


Figure 1. Top panels: synthetic curve of CME kinematics (black) together with the data (asterisks), results derived from the regularization tool (dashed blue) and the spline fit (pink). Middle panels: derived acceleration profile (black: true solution, blue: regularization tool result, pink: spline fit result). Bottom panels: normalized residuals (we note that in the left panel case the residuals make no sense due to the division by errors of the order of 0). Left panels: sampling rate is smaller than for the “true” curve, but the data are without noise. Right panels: same sampling rate as left but with noise added to the data.

We first test the reliability of the methods and derive the acceleration from the synthetic HT data without noise (Figure 1, left panels). For comparison, the right panels of Figure 1 show the results derived from HT data with noise added. We note that the second part of the synthetic curve (decreasing height) is unrealistic for a CME evolution, but the profile was used to provide a challenge to both methods. As can be seen from the left panels, without noise the outcome from the regularization tool represents the acceleration curve better than that from the spline fit with respect to the timing of the acceleration peak and the acceleration duration, though the spline fit method reproduces the HT curve quite well. The peak amplitude of the CME acceleration is well represented by the regularization tool, whereas it is underestimated (by about 20%) by the spline fit method. In addition, the regularization tool reveals horizontal error bars (± 1.0 minutes) to account for the uncertainty in timing due to the reduced sampling rate. From the right panels of Figure 1, it can be seen that the acceleration curve derived from the spline fit applied on noisy data has only slightly changed; whereas those from the regularization tool did, since it considers the information provided by the error bars to yield an adequate error estimation which we do not get from the spline fit method. Strictly speaking, as soon as we add noise to the true HT data, the “true” velocity or acceleration cannot be reproduced. So, the prime objective of any method is to provide the range of velocities/accelerations where the “true” solution should be.

Figure 2 shows the outcome for a HT curve of an impulsively accelerated CME evolution with large noise added (average error of $0.33 R_{\odot}$, i.e., larger than typically derived from real observations). We see that the acceleration peak is well represented neither by the regularization tool nor by the spline fits. However, the intrinsic errors in time which we get from the regularization tool (± 2.0 minutes) include the true solution. The overall shape, i.e., the duration of acceleration, is well represented by both methods.

Figure 3 (left panels) shows a CME evolution curve with small errors ($\pm 0.07 R_{\odot}$) and a sampling rate increasing from 2 to 10 minutes, simulating a cadence of measurement points comparable to the actual observations in the present study. The spline fit acceleration varies only little when applying different numbers of nodes (6, 7, and 8) and matches well the peak but not the duration of acceleration. The outcome of the regularization tool for the most part matches the true solution within its error bars (uncertainty in the timing of the acceleration peak about ± 3.0 minutes). The right panels of Figure 3 shows the same kinematical curve, however, with a higher sampling rate of 1 and 2 minutes, respectively. The acceleration peak derived from the spline fit using different nodes shows a larger discrepancy. The timing of the acceleration peak calculated from the regularization tool is consistent with the true curve. However, its uncertainty is estimated to about ± 4.0 minutes. To summarize, a sampling rate of ~ 2 minutes covering the impulsive acceleration phase reproduces the true curve in a reasonable way. Higher time cadence data produce a better estimate of the acceleration duration. Somewhat surprisingly, the horizontal uncertainties on the acceleration peak are larger when a higher sampling rate is used (< 2 minutes). This is due to the fact that small time steps between the HT data points with errors cause larger uncertainties in the subsequent derivative. Thus, the enhancement of the time cadence can only improve the acceleration profiles when also the errors in the CME HT measurements are reduced.

4. CME ACCELERATION COMPARED TO FLARE ENERGY RELEASE

The flare/CME events under study are 2007 June 3 (C5.3), 2007 December 31 (C8.3), and 2008 March 25 (M1.7). Figures 4, 5, and 6 show for the three events the evolution of the erupting CME in the low corona in EUVI 171 Å and

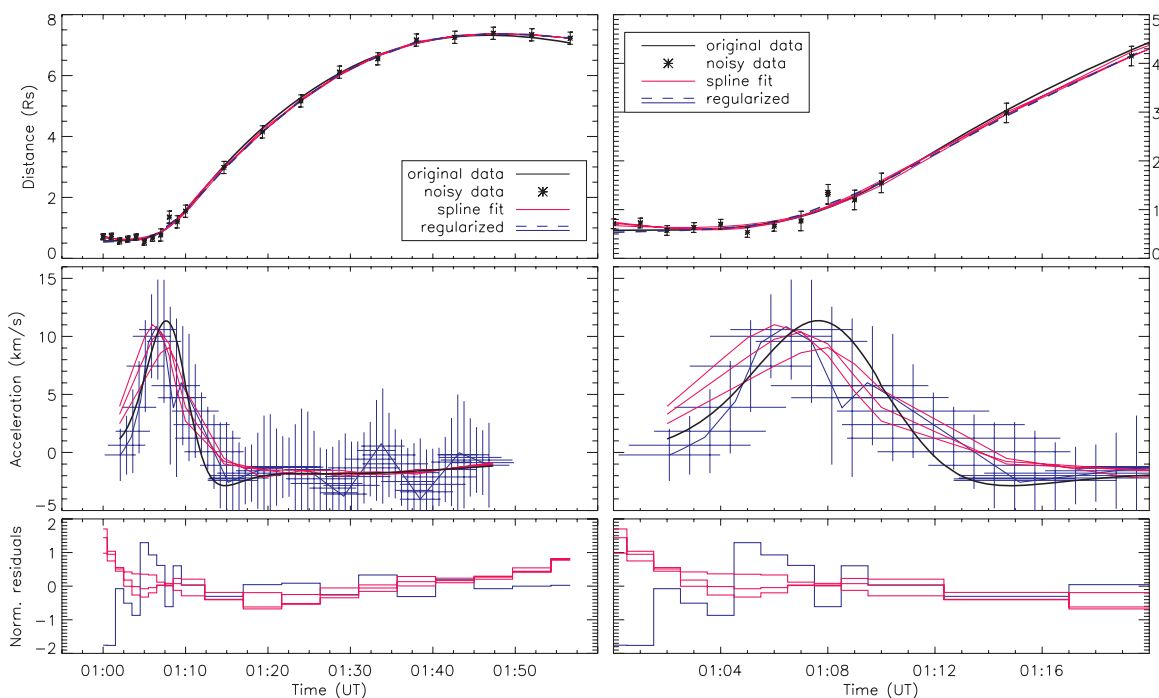


Figure 2. Top to bottom panels: same as in Figure 1. Left panels: impulsively accelerated CME evolution with rather high noise and errors. Right panels: close-up view for the time range during the peak acceleration phase.

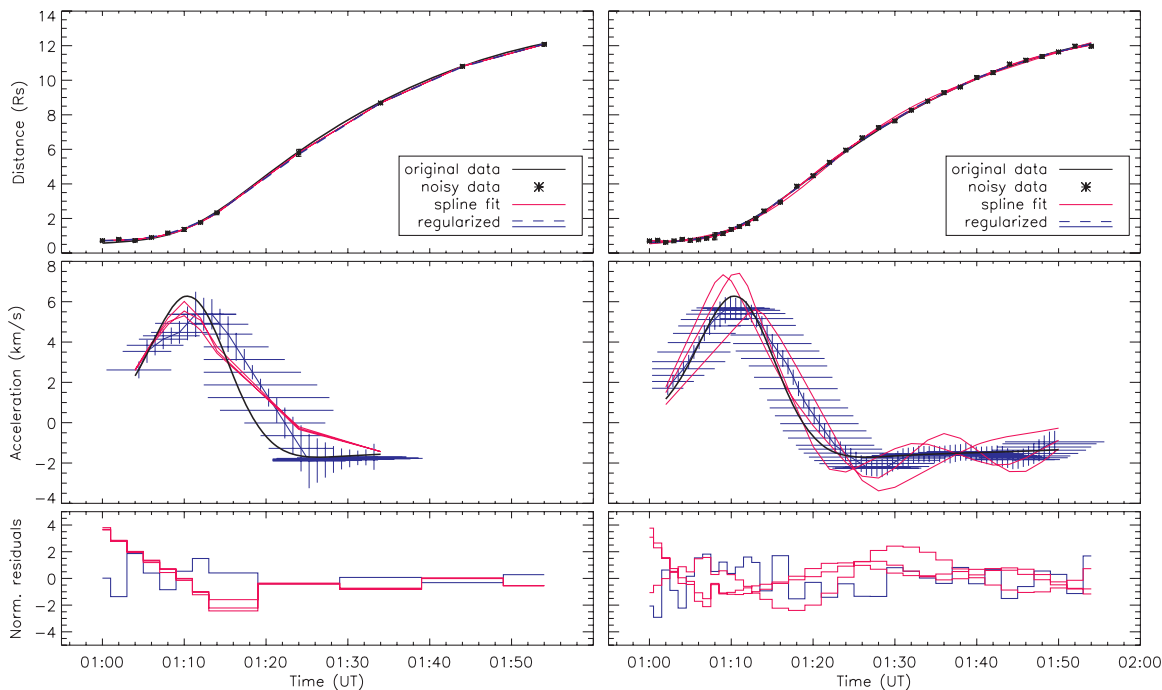


Figure 3. Top to bottom panels: same as in Figure 1. Realistic scenario of CME evolution applying low noise to the data and error bars comparable to those from the observations. Left panels: simulated is a time cadence of data points comparable to the actual observations. Right panels: same curve but with higher time cadence.

white-light images from COR1. In both instruments, we follow the leading edge of the CME as indicated by crosses in the figures. In EUVI 171 Å ($T \sim 1 \times 10^6$ K), typical CME features as the frontal rim and the cavity are observed (see also Aschwanden et al. 2009). However, the embedded cooler prominence material ($T \sim 1 \times 10^4$ K), visible in the subsequent coronagraph images, is missing. This is reasonable, since the contrast of prominences against the coronal background drops sharply for lines formed at $T \geq 3 \times 10^5$ K (Noyes et al. 1972). The

obvious similarity of the morphology and the temporal evolution of the developing/propagating CME structure justifies the link between EUV and coronagraph observations (for a discussion, see Maričić et al. 2004). By combining measurements of the leading edge of the erupting structure from EUVI and COR1 images, we derive the kinematics of the CME with typical uncertainties of ± 0.02 – $0.05 R_{\odot}$ for EUVI and $\pm 0.12 R_{\odot}$ for COR1. We stress that for each event under study, the location of the CME source (estimated by the flare position) is close

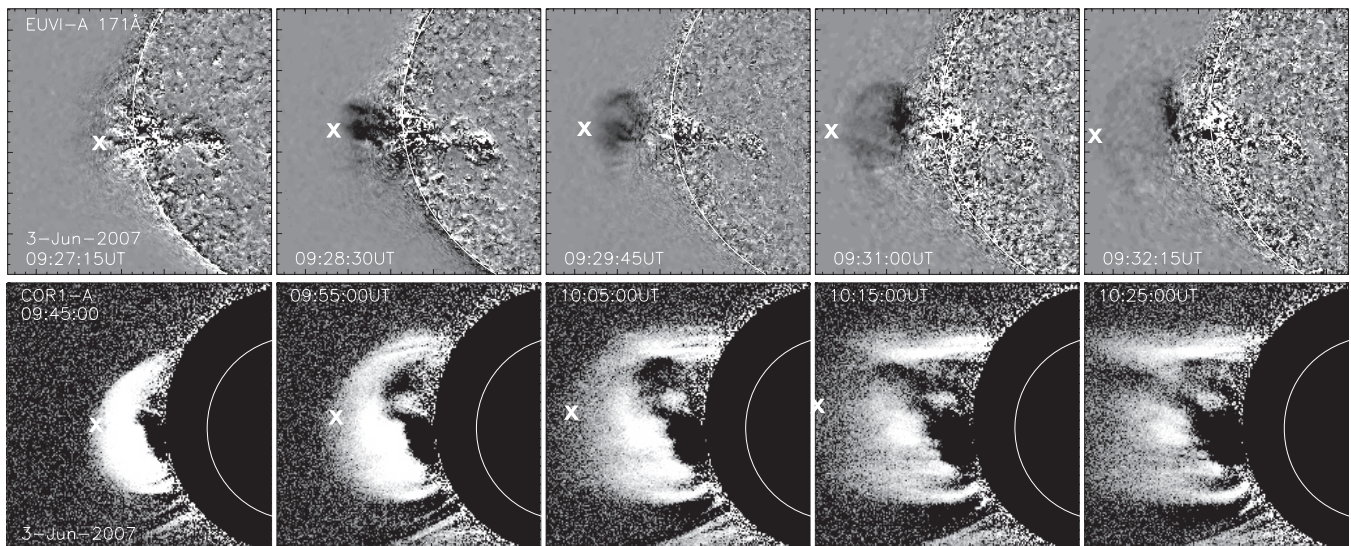


Figure 4. 2007 June 3, C5.3 flare/CME event observed with *STEREO-A*. Sequence of EUVI 171 Å running difference images and COR1 total brightness images. Crosses indicate the measured leading edge from which the CME kinematics (shown in Figure 8) is derived.

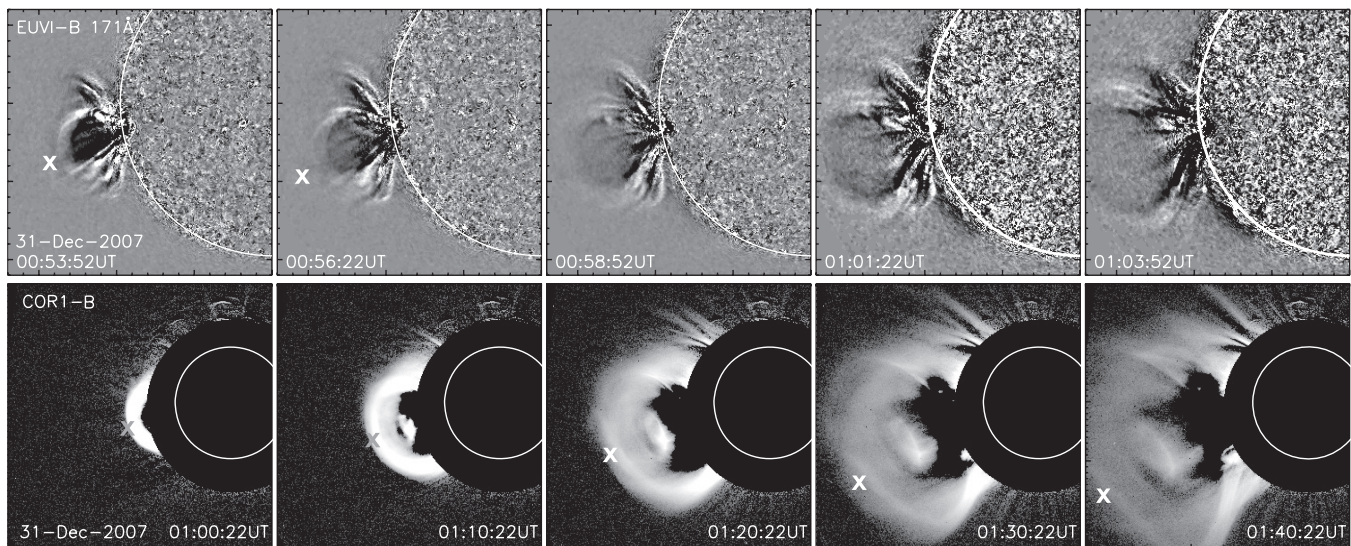


Figure 5. 2007 December 31, C8.3 (M2) flare/CME event observed with *STEREO-B*. Sequence of EUVI 171 Å running difference images and COR1 images. Crosses indicate the measured leading edge from which the CME kinematics is derived (Figure 10).

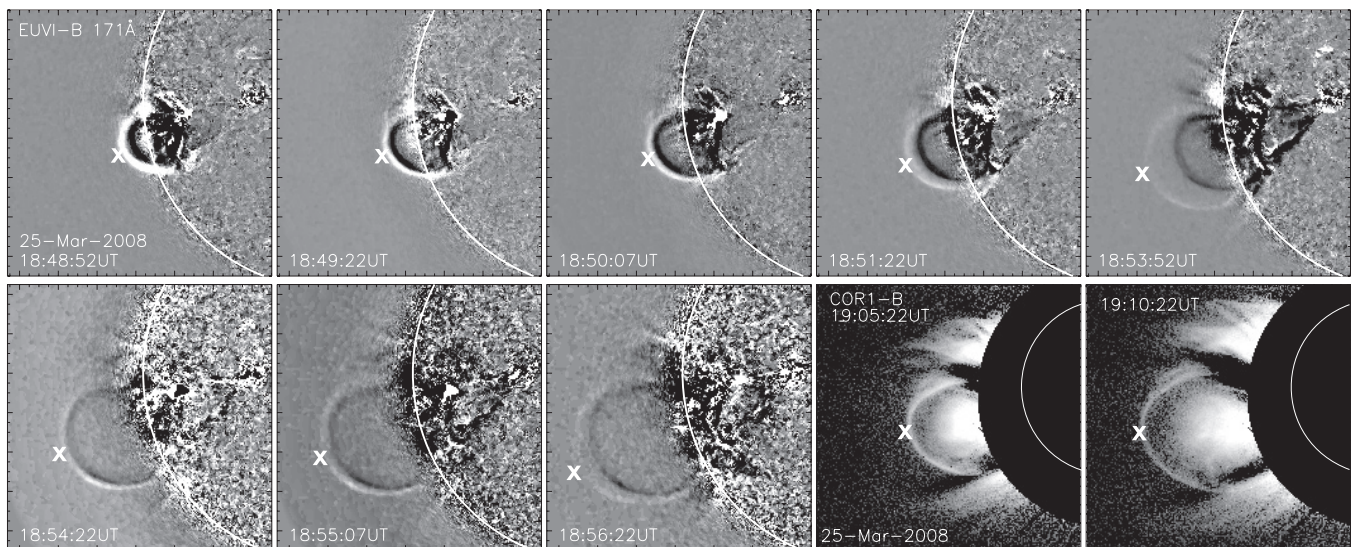


Figure 6. 2008 March 25, M1.7 flare/CME event observed with *STEREO-B*. Sequence of EUVI 171 Å running difference images and COR1 images. Crosses indicate the measured leading edge from which the CME kinematics is derived (Figure 12).

to the limb ($\pm 10^\circ$ – 25°). Thus, we expect that the influence of projection effects on the derived kinematics is small. We also note that for all events, large-scale coronal waves were detected in the EUVI 195 Å image sequences.

4.1. 2007 June 3: C5.3 Flare/CME Event

The 2007 June 3 CME event is associated with a C5.3 GOES class flare at heliographic position S08E67 (EUVI event catalog; Aschwanden et al. 2009). The position angle of *STEREO-A* with respect to Earth is 7° , hence for *STEREO-A* the CME was observed $\sim 16^\circ$ off the spacecraft plane-of-sky. The event was observed by EUVI with a high cadence of 75 s.

Figure 7 shows the *RHESSI* HXR image (top panel) reconstructed in the energy band 30–50 keV with the CLEAN algorithm (Hurford et al. 2002) together with its spectrum (bottom panel) integrated over 20 s around the peak of the HXR emission. The spectrum was fitted with a thermal plus non-thermal model in the energy range 6–200 keV. The HXR source, located close to the eastern limb, is compact with some indication of two footpoints (but not clearly resolved). From the *RHESSI* spectral fit, we derive a photon spectral index $\gamma = 2.4$ which indicates a very flat (i.e., hard) spectrum and a photon flux density at 50 keV during the event peak, $F_{50} = 0.93$ photons $\text{s}^{-1} \text{cm}^{-2} \text{keV}^{-1}$.

Figure 8 shows the CME distance, velocity, and acceleration time-profiles for the distance range 1.0–3.3 R_\odot (left panels from top to bottom). To enlarge the details on the impulsive acceleration phase, the right panels of Figure 8 show the same curves but for the distance range up to 1.7 R_\odot . For comparison, the *RHESSI* HXR flux of the associated flare in the energy range 30–50 keV is overplotted in the bottom panels of Figure 8. *RHESSI* reveals impulsive and powerful HXR emission with a distinct burst of short duration (less than 2 minutes). The evolution of the acceleration profile of the CME and the evolution of the flare HXR flux are highly synchronized peaking at 09:27 UT with an uncertainty of ± 1.25 minutes (CME) and 09:27:14 UT (*RHESSI* 30–50 keV HXR flux). The CME reveals a large peak velocity (~ 1170 km s^{-1}) and peak acceleration (~ 5.1 km s^{-2}), which occur within the EUVI FoV, i.e., below 1.7 R_\odot . The CME accelerates within 8 minutes up to ~ 1170 km s^{-1} , then drops within the next 2 minutes down to a velocity of ~ 700 km s^{-1} and further decelerates over the following 10 minutes until reaching a constant velocity of ~ 500 km s^{-1} . If one determined the CME speed solely from coronagraph observations, the velocity peak would be missed.

4.2. 2007 December 31: C8.3 Flare/CME Event

The 2007 December 31 CME event is associated with a C8.3 GOES class flare. The source region lies behind the limb at roughly S09E102 (Krucker et al. 2010; Dai et al. 2010), which makes this event special with respect to observations from Earth-view (*GOES* and *RHESSI*). From the *RHESSI* perspective, the footpoints of the flare are occulted, and we actually observe a coronal HXR source at non-thermal energies, with a good count statistics in the range 20–50 keV. This might be interpreted as Masuda-type source (Masuda et al. 1994). For that day, *MESSENGER* (Solomon et al. 2001) is at a heliographic longitude of about E165 and observed the non-occulted flare in SXR (similar to *GOES*). The flux measured by *MESSENGER* is about 2.8 times higher than the flux observed by *GOES* which makes the flare actually of M2 class (Krucker et al. 2010).

Figure 9 shows the *RHESSI* HXR image reconstructed in the energy band 20–50 keV (top panel) together with its spectrum

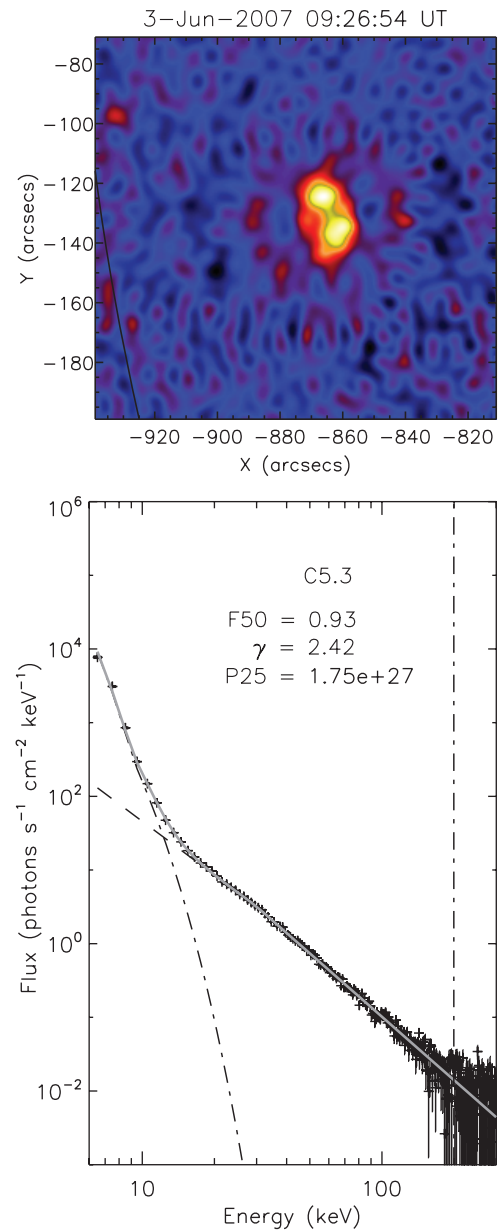


Figure 7. 2007 June 3 C5.3 flare. Top panel: *RHESSI* 30–50 keV HXR image integrated over 20 s around the flare peak using front detectors 2–8 (except 5 and 7) reconstructed with the CLEAN algorithm. Bottom panel: *RHESSI* spectrum and fit components for the energy range 6–200 keV. The isothermal fit is indicated as dash-dotted line, the non-thermal power-law fit as dashed line, and the sum of both components as thick gray line. The derived parameters, electron flux density at 50 keV F_{50} (photons $\text{s}^{-1} \text{cm}^{-2} \text{keV}^{-1}$), photon spectral index γ , and power P_{25} (erg s^{-1}) in electrons above a cutoff energy of 25 keV are given in the legend.

(bottom panel) integrated over 20 s around the peak of the HXR emission and fitted in the energy range 6–90 keV. The image reveals that the strongest HXR emission comes from above the eastern limb, hence the footpoints of the flare are occulted. This means that the HXR flux entirely originates from the coronal source (e.g., Krucker et al. 2008). For this event, we derive the *RHESSI* spectral fit parameters as $\gamma = 4.5$, which means a softer HXR spectrum compared to the previous event, and $F_{50} = 0.17$ photons $\text{s}^{-1} \text{cm}^{-2} \text{keV}^{-1}$. The considerably lower photon flux density and the softer spectrum as compared to the 2007 June 3 event are not surprising, since loop-top sources are generally less bright than the footpoints (Krucker & Lin 2008).

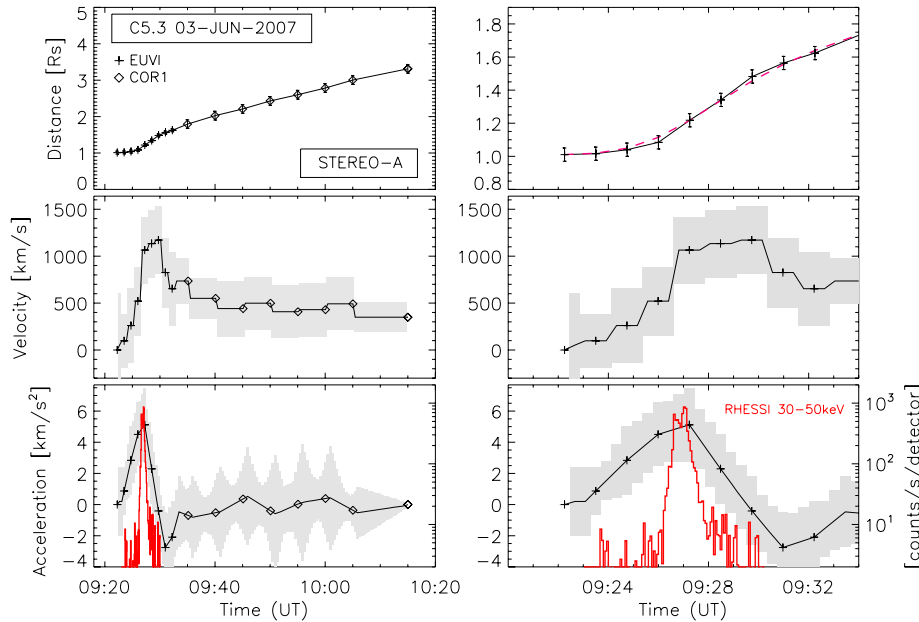


Figure 8. CME kinematics for the 2007 June 3 C5.3 flare/CME event. Top to bottom panels: CME distance, velocity, and acceleration against time together with the background-subtracted flare HXR flux (red). Left panels: full height range; right panels: close-up view onto the early evolution phase. The pink dashed line in the right top panel (CME distance–time measurements) shows the regularized solution returned from the inversion technique. The gray shaded area in the CME velocity and acceleration curves indicates the 95% confidence level.

At that day, *STEREO-B* had a position angle of 23° with respect to Earth, hence the CME was observed 11° off the *STEREO-B* plane-of-sky. Figure 10 shows the CME distance–time, velocity, and acceleration profile for the measured distance range $1\text{--}5 R_\odot$ (left panels). The close-up view (right panels) shows the distance range up to $2.5 R_\odot$. We stress that for this event one data point (COR1) in the overlapping FoVs of EUVI and COR1 ($1.4\text{--}1.7 R_\odot$) reveals a shift between both the instruments, but which lies within the applied error bars. The CME reaches a maximum velocity of $\sim 790 \text{ km s}^{-1}$ within <10 minutes with a maximum acceleration of $\sim 1.3 \text{ km s}^{-2}$. The impulsive acceleration phase of the CME is finished within the EUVI FoV and shows a peak at 00:50 UT (± 2.5 minutes) which (within the uncertainties) is in accordance with the HXR evolution and peak time at 00:47:48 UT (Figure 10, bottom panels). This is particularly interesting, as in this event we do not observe the HXR emission from the footpoints (which are occulted) but from a coronal source.

4.3. 2008 March 25: M1.7 Flare/CME Event

The 2008 March 25 CME event is associated with a M1.7 *GOES* class flare. The source region lies at S10E87 (EUVI event catalog; Aschwanden et al. 2009), and the position angle of *STEREO-B* with respect to Earth is 24° , i.e., the CME propagates about 27° off the *STEREO-B* plane-of-sky. The event is observed with high cadence by EUVI and COR1 (75 s and 5 minutes, respectively). *RHESSI* observed the peak phase of the flare HXR emission but missed part of the rising phase due to spacecraft night.

Figure 11 shows the *RHESSI* HXR image in the energy band 18–30 keV (top panel) together with its spectrum (bottom panel) integrated over 20 s around the peak of the HXR emission. The spectrum was fitted in the energy range 6–100 keV, giving $\gamma = 3.5$ and $F_{50} = 0.23 \text{ photons s}^{-1} \text{ cm}^{-2} \text{ keV}^{-1}$. The image shows a rather compact source of HXR emission, revealing a weaker component in the corona in addition to the on-disk footpoint emission; and suggesting that the second footpoint

lies occulted behind the eastern limb (the energy range 18–30 keV is dominated by non-thermal emission, see spectrum in Figure 11). In EUVI 304 Å images, a bright ejection is observed which may coincide with the coronal *RHESSI* source.

STEREO-B EUVI running difference and COR1 images (Figure 6) reveal a very thin and distinct spherically shaped front of the CME, reminding one of the cross section of a flux rope torus. This shape is maintained in COR1 white-light images (also see Aschwanden et al. 2009). The distance–time, velocity, and acceleration profiles are shown in Figure 12, overplotted with the *RHESSI* HXR flux in the energy range 18–30 keV. The COR1 data point lying in the overlapping FoVs of EUVI and COR1 fits well to the CME HT data measured by EUVI. Due to *RHESSI* night, the initial flare phase is missed, but the peak is clearly observed. *RHESSI* comes out of spacecraft night at $\sim 18:44$ UT revealing enhanced HXR emission with a maximum at 18:51:34 UT. The CME velocity starts to increase at 18:35 UT, the acceleration reaching a peak at 18:50 UT (± 3.5 minutes). We note that the acceleration time-profile shows two acceleration steps within the EUVI FoV. The CME reaches a peak velocity of 970 km s^{-1} within ~ 20 minutes with an acceleration maximum of $\sim 1 \text{ km s}^{-2}$.

5. SUMMARY AND DISCUSSION

Both the spline fit and the regularization tool determine the acceleration phase of a CME (peak and duration) reasonably well. The main plus of the regularization tool over the spline fit method is the provision of errors in time and amplitude. In all test cases, the true solution was included within this error estimation. We come to the somewhat surprising result that an increased image cadence (<2 minutes) does not reduce the uncertainty in determining the peak time of CME acceleration. This is due to the measurement errors of the CME leading edge. The inconsistencies of the CME leading edge as measured in different wavelength regimes (EUV and white light) as well as the change of intensity over the FoV of a single instrument do not allow us to narrow the measurement errors. The same

Table 1
Summary of the CME and Flare Characteristics for Each Event

| Date (dd-mm-yy) | Class | Δt | v_{\max} (h) | a_{\max} (h) | F_{50} | γ | P_{25} |
|-----------------|-------|------------|-----------------------|----------------------|----------|----------|----------|
| 03-Jun-07 | C5.3 | 0.1 | 1171 ± 359 (0.48) | 5.1 ± 2.4 (0.26) | 0.93 | 2.4 | 1.75 |
| 31-Dec-07 | C8/M2 | 2.0 | 785 ± 125 (2.10) | 1.3 ± 0.4 (0.25) | 0.17 | 4.5 | 4.09 |
| 25-Mar-08 | M1.7 | 1.5 | 967 ± 173 (1.97) | 1.0 ± 0.2 (0.40) | 0.23 | 3.5 | 1.88 |

Notes. We give the date, the *GOES* flare class, the difference Δt (minutes) between CME peak acceleration and flare HXR peak, the derived CME peak velocity v_{\max} (km s^{-1}) and peak acceleration a_{\max} (km s^{-2}) with errors (95% confidence level), the CME height h (R_{\odot}) from the source region, the electron flux density at 50 keV, F_{50} ($\text{photons s}^{-1} \text{cm}^{-2} \text{keV}^{-1}$), the flare HXR spectral slope γ , and the total power in electrons P_{25} ($10^{27} \text{erg s}^{-1}$).

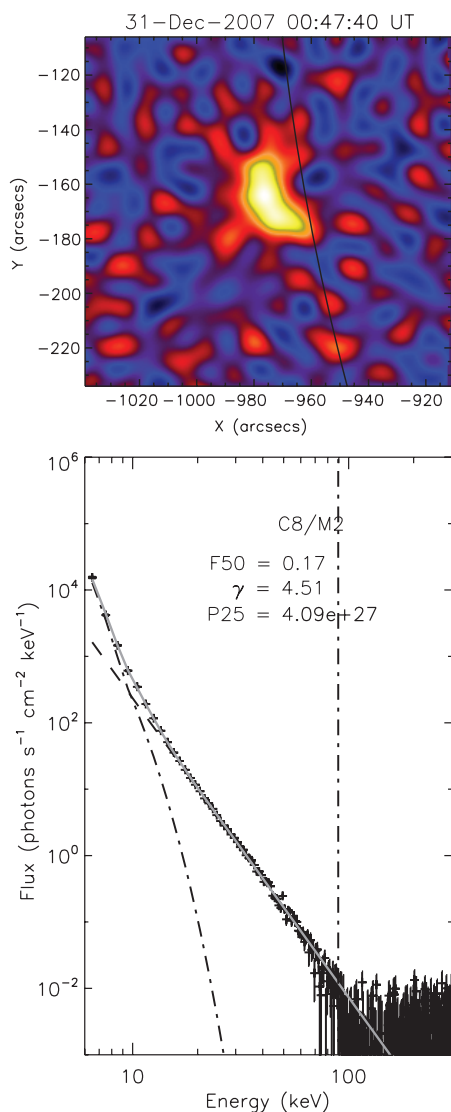


Figure 9. Same as in Figure 7, but for the 2007 December 31 C8.3 (M2) flare. The HXR image is integrated over the energy band 20–50 keV.

holds for the acceleration amplitude for which the uncertainties lie in the range between 10% and 50%. As a check for the goodness of the obtained velocity and acceleration profiles from the regularization tool, the normalized residuals between the regularized solutions and the distance–time measurements are investigated and found to be small (≤ 1.5).

Table 1 summarizes the relevant parameters derived from the CME and flare. From the three events under study, we obtain that the peak acceleration of the CME is reached within a few minutes after its launch and at low distances of $\leq 0.4 R_{\odot}$

from the flare site, which we use as an estimate of the CME source region location. We would like to note that all events occurred close to the limb. Thus, projection effects are small, and the derived values should be close to the “true” ones. In these events, the impulsive acceleration phase is already finished before the CME is observed in the coronagraph COR1 FoV. The peak velocity of the CME is reached within heights of $< 2.2 R_{\odot}$ above the source region. The CME acceleration profile and the flare HXR emission are highly synchronized and peak almost simultaneously. The differences between the flare HXR peak and the CME acceleration peak are in the range $\Delta t \leq 2$ minutes. Such differences lie within the limitations for deriving the CME acceleration peak time, which are caused by the finite cadence and measurement errors in the HT measurements. The uncertainties in the peak time of the CME acceleration estimated from the inversion method lie in the range 2–3.5 minutes (see Section 3).

We note that there is no clear relation between CME velocity and *GOES* class of the associated flare. For the events under study these parameters vary only by a factor of ~ 2 . Statistical studies comparing the flare SXR peak flux and CME peak velocity find a linear correlation coefficient of about $r \sim 0.47$, which is not very strong (Moon et al. 2002). However, in our three events there seems to be a correlation indicated between the CME acceleration peak and the flare HXR peak flux, both of which vary over a factor of 5 in the three events under study. Also, some relation between the spectral slope of the HXR spectra and the CME acceleration is suggested (harder flare spectrum seems to be related to larger CME acceleration). Of course, three events are inconclusive for such a relationship, but our results suggest that this should be tested on a larger event sample.

Especially for the 2007 June 3 event, intriguing results are derived. The single HXR burst of only ~ 2 minute duration goes along with a rather high HXR flux density, CME peak acceleration (acceleration phase of ~ 8 minutes), and a very hard HXR spectrum. In contrast to that, a relatively low total energy in flare-accelerated electrons and low *GOES* classification is revealed. Further, the 2007 June 3 CME shows quite unusual behavior with respect to its very strong deceleration profile with values of -3 km s^{-2} and the velocity decreases from 1100 km s^{-1} to 500 km s^{-1} very low in the corona ($< 0.5 R_{\odot}$). Typical CME deceleration values are in the order of -0.01 to -0.1 km s^{-2} (e.g., Vršnak et al. 2004) and are due to the interaction with the solar wind flow. After the magnetic driving force of the eruption ceases, the CME is slowed down by the drag force until its velocity adjusts to the speed of the solar wind (e.g., Cargill 2004; Manoharan 2006; Vršnak et al. 2008; and references therein). Reeves (2006) studied the relationship between the CME acceleration and the thermal energy release rate in a loss-of-equilibrium flux rope model (e.g., Lin & Forbes

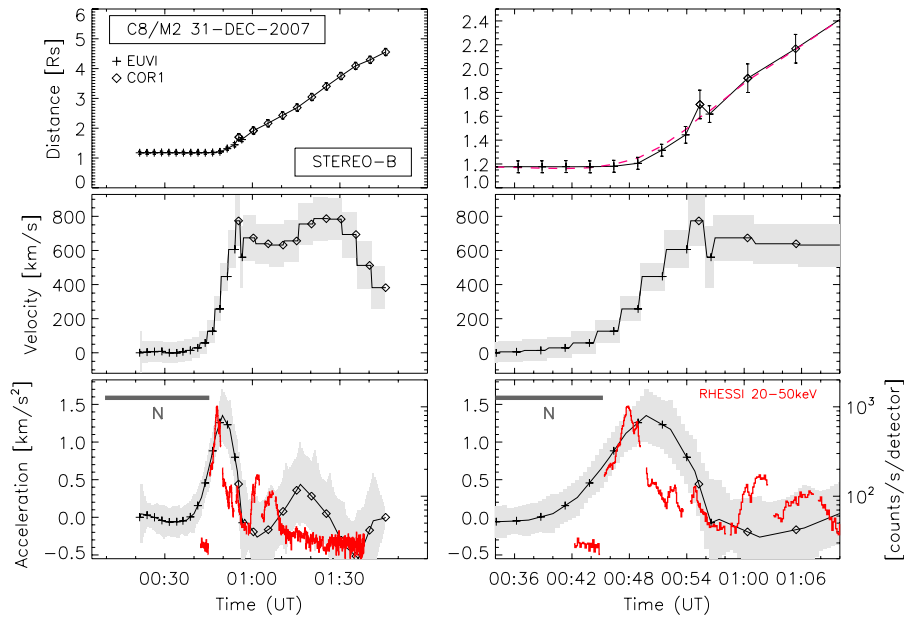


Figure 10. Same as Figure 8, but for the 2007 December 31 C8.3 (M2) flare/CME event. The gray bar indicates the time range of *RHESSI* night (N).

2000; Lin 2002). They found that for high background magnetic fields and fast reconnection rates, the evolution of the CME acceleration and flare energy release rate are well correlated. Reeves (2006) also points out that due to rapid reconnection the formation of a long current sheet in the wake of a CME is prevented and consequently the energy release is inhibited. For the 2007 June 3 event, we therefore assume a localized strong magnetic field from which the CME erupts as well as strong overlying fields. On the one side this yields high reconnection rates over a short time range, on the other side a strong overlying magnetic field would drastically decelerate the CME at low coronal heights.

Well-observed flare/CME events close to the limb, such as presented in this study, are less affected by projection effects when analyzing the CME parameters and enable us to reliably determine its kinematics and acceleration values. However, close to the limb the associated flare is observed either as “classical” on-disk HXR emitting source (footpoints of flare loops at chromospheric heights) or as coronal loop-top emission only, when the bright footpoint emission is occulted by the solar limb. In partially disk-occulted events, loop-top sources could be studied on a statistical basis (e.g., Krucker & Lin 2008); and it is most probable that they are related to the initial location of particle acceleration (e.g., Krucker et al. 2008). Battaglia & Benz (2006) studied five *RHESSI* flares where HXR emission from both footpoints and the loop-top was observed. They found that the coronal and footpoint sources are well correlated with respect to their temporal and spectral evolution. Our results show in fact that the CME acceleration peak phase is well correlated with both types of HXR sources, i.e., coronal and footpoint HXR emission of the associated flare.

In the present study, we found for all three events under study that the impulsive acceleration of the CME is finished at distances of $\leq 0.4 R_{\odot}$ above the solar surface, i.e., within the EUVI FoV and before reaching the COR1 FoV. Hence, from coronagraphic observations only, the early CME evolution may be considerably misinterpreted. Vrřnak (1990) and Chen & Krall (2003) obtained from analytical models, in which CMEs are treated as toroidal field structures, that the peak of the acceleration should be reached when the half-

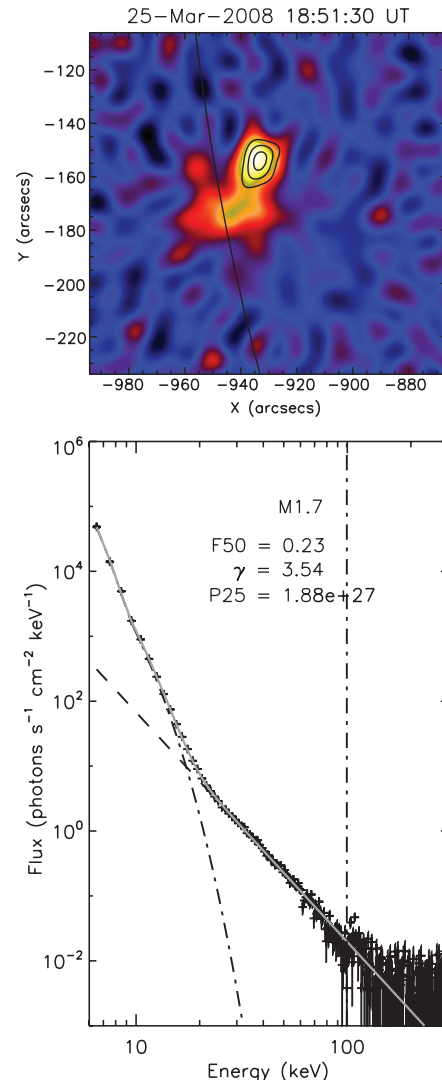


Figure 11. Same as in Figure 7, but for the 2008 March 25 M1.7 flare. The HXR image is integrated over the energy band 18–30 keV. Contours show levels of 50%, 70%, and 90% of maximum emission for the energy band 30–50 keV.

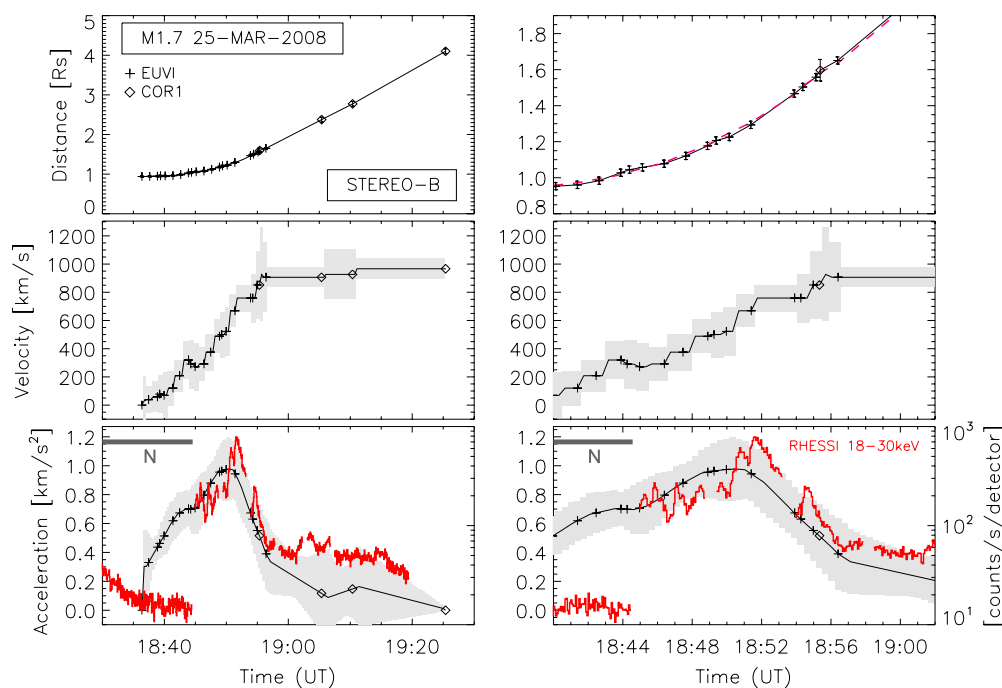


Figure 12. Same as Figure 8, but for the 2008 March 25 M1.7 flare/CME event. The gray bar indicates the time range of *RHESSI* night (N).

separation of the CME footpoints is comparable to the CME height above the flare site. For the 2008 March 25 event, the CME footpoint separation can be derived with adequate accuracy (see Figure 5). We obtained a CME half-separation of $\sim 210 \pm 30$ Mm, which is comparable to its peak height of ~ 280 Mm.

Our results point to a possible relation between the flare HXR spectra and the CME acceleration (the event with the highest CME acceleration has the highest HXR flux density and flattest spectrum) whereas the relation to the peak power in electrons and the GOES SXR peak flux seems weak. Maričić et al. (2007) pointed out that the reconnection rate is more relevant for the CME acceleration than a strong heating and non-thermal particle acceleration. From our results, it seems that the efficiency of accelerating particles to high energies is better correlated to the CME acceleration than the total number and energy in electrons (though we note that more statistics on this is needed). Such results may provide new constraints on electron acceleration models and its magnetic geometry as the particle acceleration mechanism has to go along with a rapid closing of magnetic field lines which is needed to drive the CME.

6. CONCLUSIONS

The present study based on high cadence data from *STEREO*-EUVI, *STEREO*-COR1, and *RHESSI* evidences a very close relation between flares and CMEs. From three well-observed impulsive events that occurred close to the limb, we derive that the CME acceleration profile and energy release of the associated flare evolve in a synchronized manner. This supports the “standard” flare/CME model which predicts a feedback relationship between the large-scale CME acceleration and the energy release process in the associated flare (e.g., Lin 2004; Maričić et al. 2007; Temmer et al. 2008; Vršnak & Cliver 2008): After the magnetic structure loses equilibrium and starts rising, a current sheet is formed below the rising structure (presumably a flux rope), becoming a site of magnetic field reconnection. The reconnection has two important consequences for the CME

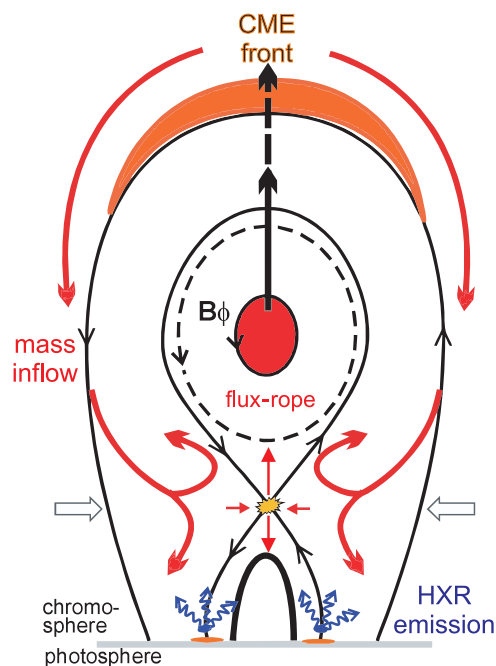


Figure 13. Illustration of the flare-CME feedback mechanism between the large-scale CME dynamics and small-scale flare processes. The upward moving CME evacuates the area in its wake, boosting mass inflow from aside into the reconnection region. The more mass and frozen-in magnetic field is transported into the region, the higher is the magnetic reconnection rate leading to larger flare energy release and to more efficient acceleration of particles. The successive closing of magnetic field lines due to reconnection increases the poloidal flux B_ϕ in the eruption, which leads to a stronger upward oriented magnetic driving force (Lorentz force).

acceleration: it reduces the downward-acting tension of the overlying field (Lin 2004), and it supplies additional poloidal flux to the flux rope (Vršnak 2008), which is considered to be the main driver of the eruption (e.g., Chen 1989; Vršnak 1990; Chen 1996; Kliem & Török 2006; Subramanian & Vourlidis 2007).

On the other hand, the upward moving CME drives mass inflow into the current sheet, driving further magnetic reconnection and particle acceleration (see the cartoon in Figure 13). Thus, reconnection directly relates the CME acceleration and the energy release in the associated flare, leading to the close synchronization of these two phenomena.

The results from the presented study provide strong evidence for the feedback mechanism between the flare energy release and the CME acceleration. In our study, all events were fast eruptions; hence, we cannot draw conclusions on other types of eruptions (failed eruptions or gradual CMEs without flares). According to model calculations by Reeves (2006), a good correlation (within 2 minutes) between the flux rope acceleration and thermal energy release rate is expected for fast reconnection events with high background magnetic fields. This should relate to impulsive and strong events, whereas no synchronization is expected for weak and gradual events. Finally, we note that high cadence observations of CMEs in non-coronagraphic images enable us to study in detail the CME impulsive acceleration phase revealing peak acceleration as high as $\sim 5 \text{ km s}^{-2}$ even for C-class flare events. We also note that the height of the CME peak acceleration in such impulsive events is much lower ($\leq 0.4 R_{\odot}$) than previously assumed.

The authors appreciate and thank the anonymous referee for his/her constructive comments and suggestions. We thank the *STEREO* and *RHESSI* teams for their open data policy. M.T. is a recipient of an APART-fellowship of the Austrian Academy of Sciences at the Institute of Physics, University of Graz (APART 11262). A.V. acknowledges the Austrian Science Fund (FWF): P20867-N16. E.P.K. work was supported by a STFC Rolling Grant and STFC Advanced Fellowship. The European Community's Seventh Framework Programme (FP7/2007-2013) under grant agreement no. 218816 (SOTERIA) is acknowledged.

REFERENCES

- Aschwanden, M. J., Wuelser, J. P., Nitta, N. V., & Lemen, J. R. 2009, *Sol. Phys.*, **256**, 3
- Battaglia, M., & Benz, A. O. 2006, *A&A*, **456**, 751
- Brown, J. C. 1971, *Sol. Phys.*, **18**, 489
- Cargill, P. J. 2004, *Sol. Phys.*, **221**, 135
- Chen, J. 1989, *ApJ*, **338**, 453
- Chen, J. 1996, *J. Geophys. Res.*, **101**, 27499
- Chen, J., & Krall, J. 2003, *J. Geophys. Res. (Space Phys.)*, **108**, 1410
- Dai, Y., Auchère, F., Vial, J., Tang, Y. H., & Zong, W. G. 2010, *ApJ*, **708**, 913
- Fletcher, L., & Hudson, H. 2001, *Sol. Phys.*, **204**, 69
- Forbes, T. G. 2000, *J. Geophys. Res.*, **105**, 23153
- Gallagher, P. T., Lawrence, G. R., & Dennis, B. R. 2003, *ApJ*, **588**, L53
- Groetsch, C. W. 1984, *Research Notes in Mathematics* (Boston, MA: Pitman), 105
- Hanke, M., & Scherzer, O. 2001, *Am. Math. Mon.*, **108**, 512
- Howard, R. A., et al. 2008, *Space Sci. Rev.*, **136**, 67
- Hudson, H. S., Acton, L. W., Hirayama, T., & Uchida, Y. 1992, *PASJ*, **44**, L77
- Hurford, G. J., et al. 2002, *Sol. Phys.*, **210**, 61
- Kaiser, M. L., Kucera, T. A., Davila, J. M., St. Cyr, O. C., Guhathakurta, M., & Christian, E. 2008, *Space Sci. Rev.*, **136**, 5
- Kliem, B., & Török, T. 2006, *Phys. Rev. Lett.*, **96**, 255002
- Kontar, E. P., & MacKinnon, A. L. 2005, *Sol. Phys.*, **227**, 299
- Kontar, E. P., Piana, M., Massone, A. M., Emslie, A. G., & Brown, J. C. 2004, *Sol. Phys.*, **225**, 293
- Krucker, S., Hudson, H. S., Glesener, L., White, S. M., Masuda, S., Wuelser, J.-P., & Lin, R. P. 2010, *ApJ*, submitted
- Krucker, S., & Lin, R. P. 2008, *ApJ*, **673**, 1181
- Krucker, S., et al. 2008, *A&AR*, **16**, 155
- Lin, J. 2002, *Chin. J. Astron. Astrophys.*, **2**, 539
- Lin, J. 2004, *Sol. Phys.*, **219**, 169
- Lin, R. P., Dennis, B. R., Hurford, G. J., Smith, D. M., & the RHESSI team 2002, *Sol. Phys.*, **210**, 3
- Lin, J., & Forbes, T. G. 2000, *J. Geophys. Res.*, **105**, 2375
- MacQueen, R. M., & Fisher, R. R. 1983, *Sol. Phys.*, **89**, 89
- Manoharan, P. K. 2006, *Sol. Phys.*, **235**, 345
- Maričić, D., Vršnak, B., Stanger, A. L., & Veronig, A. 2004, *Sol. Phys.*, **225**, 337
- Maričić, D., Vršnak, B., Stanger, A. L., Veronig, A. M., Temmer, M., & Roša, D. 2007, *Sol. Phys.*, **241**, 99
- Masuda, S., Kosugi, T., Hara, H., Tsuneta, S., & Ogawara, Y. 1994, *Nature*, **371**, 495
- Moon, Y.-J., Choe, G. S., Wang, H., Park, Y. D., Gopalswamy, N., Yang, G., & Yashiro, S. 2002, *ApJ*, **581**, 694
- Noyes, R. W., Dupree, A. K., Huber, M. C. E., Parkinson, W. H., Reeves, E. M., & Withbroe, G. L. 1972, *ApJ*, **178**, 515
- Reeves, K. K. 2006, *ApJ*, **644**, 592
- Schwartz, R. A., Csillaghy, A., Tolbert, A. K., Hurford, G. J., McTiernan, J., & Zarro, D. 2002, *Sol. Phys.*, **210**, 165
- Solomon, S. C., et al. 2001, *Planet. Space Sci.*, **49**, 1445
- St. Cyr, O. C., Burkepile, J. T., Hundhausen, A. J., & Lecinski, A. R. 1999, *J. Geophys. Res.*, **104**, 12493
- Subramanian, P., & Vourlidas, A. 2007, *A&A*, **467**, 685
- Temmer, M., Veronig, A. M., Vršnak, B., Rybák, J., Gömöry, P., Stoiser, S., & Maričić, D. 2008, *ApJ*, **673**, L95
- Thompson, W. T., et al. 2003, *Proc. SPIE*, **4853**, 1
- Vršnak, B. 1990, *Sol. Phys.*, **129**, 295
- Vršnak, B. 2001, *J. Geophys. Res.*, **106**, 25249
- Vršnak, B. 2008, *Ann. Geophys.*, **26**, 3089
- Vršnak, B., & Cliver, E. W. 2008, *Sol. Phys.*, **253**, 215
- Vršnak, B., Maričić, D., Stanger, A. L., Veronig, A. M., Temmer, M., & Roša, D. 2007, *Sol. Phys.*, **241**, 85
- Vršnak, B., Ruždjak, D., Sudar, D., & Gopalswamy, N. 2004, *A&A*, **423**, 717
- Vršnak, B., Vrbanec, D., & Čalogović, J. 2008, *A&A*, **490**, 811
- Wen, Y., Maia, D. J. F., & Wang, J. 2007, *ApJ*, **657**, 1117
- Wuelser, J.-P., et al. 2004, *Proc. SPIE*, **5171**, 111
- Zhang, J., & Dere, K. P. 2006, *ApJ*, **649**, 1100
- Zhang, J., Dere, K. P., Howard, R. A., Kundu, M. R., & White, S. M. 2001, *ApJ*, **559**, 452
- Zhang, J., Dere, K. P., Howard, R. A., & Vourlidas, A. 2004, *ApJ*, **604**, 420